

Article

Microstructure, Mechanical, and Corrosion Behavior of Al₂O₃ Reinforced Mg₂Zn Matrix Magnesium Composites

Ali Ercetin ^{1,*}  and Danil Yurievich Pimenov ^{2,*} 

¹ Department of Mechanical Engineering, Faculty of Engineering and Architecture, Bingol University, Bingol 12000, Turkey

² Department of Automated Mechanical Engineering, South Ural State University, Lenin Prosp. 76, 454080 Chelyabinsk, Russia

* Correspondence: aliercetin@bingol.edu.tr (A.E.); danil_u@rambler.ru (D.Y.P.)

Abstract: Powder metallurgy (PM) method is one of the most effective methods for the production of composite materials. However, there are obstacles that limit the production of magnesium matrix composites (MgMCs), which are in the category of biodegradable materials, by this method. During the weighing and mixing stages, risky situations can arise, such as the exposure of Mg powders to oxidation. Once this risk is eliminated, new MgMCs can be produced. In this study, a paraffin coating technique was applied to Mg powders and new MgMCs with superior mechanical and corrosion properties were produced using the hot pressing technique. The content of the composites consist of an Mg₂Zn matrix alloy and Al₂O₃ particle reinforcements. After the debinding stage at 300 °C, the sintering process was carried out at 625 °C under 50 MPa pressure for 60 min. Before and after the immersion process in Hank's solution, the surface morphology of the composite specimens was examined by scanning electron microscopy (SEM) and energy dispersive spectroscopy (EDS) analysis. With the hot pressing technique, composite specimens with a very dense and homogeneous microstructure were obtained. While Al₂O₃ reinforcement improved the mechanical properties, it was effective in changing the corrosion properties up to a certain extent (2 wt.% Al₂O₃). The highest tensile strength value of approximately 191 MPa from the specimen with 8 wt.% Al₂O₃. The lowest weight loss and corrosion rate were obtained from the specimen containing 2 wt.% Al₂O₃ at approximately 9% and 2.5 mm/year, respectively. While the Mg(OH)₂ structure in the microstructure formed a temporary film layer, the apatite structures containing Ca, P, and O exhibited a permanent behavior on the surface, and significantly improved the corrosion resistance.

Keywords: metal matrix composites (MMCs); magnesium matrix composites (MgMCs); microstructure; mechanical properties; corrosion; powder metallurgy; hot pressing method



Citation: Ercetin, A.; Pimenov, D.Y. Microstructure, Mechanical, and Corrosion Behavior of Al₂O₃ Reinforced Mg₂Zn Matrix Magnesium Composites. *Materials* **2021**, *14*, 4819. <https://doi.org/10.3390/ma14174819>

Academic Editor: Pavel Lukáč

Received: 7 July 2021

Accepted: 23 August 2021

Published: 25 August 2021

Publisher's Note: MDPI stays neutral with regard to jurisdictional claims in published maps and institutional affiliations.



Copyright: © 2021 by the authors. Licensee MDPI, Basel, Switzerland. This article is an open access article distributed under the terms and conditions of the Creative Commons Attribution (CC BY) license (<https://creativecommons.org/licenses/by/4.0/>).

1. Introduction

State-of-the-art biomaterials help a living structure within the body to accomplish, enhance, or substitute its natural function. They can form all or part of the living structure, as needed. The most important feature of a biomaterial is that it is biocompatible. In other words, it is non-toxic [1] and does not harm living tissues in the area where it is used [2]. Ti6Al4V, CoCr, stainless steel, platinum, and the like, which are permanent biomaterials [3], pose minimal danger in the body as they dissolve in the body at very low level [4]. However, when these materials are applied temporarily, such as implants [5], they must be removed from the body by a second surgical operation when the diseased area heals [6]. In addition, these biomaterials traditionally used metallic materials, which often exhibit unsatisfactory results such as stress protection, metal ion release, or allergic reaction. When the implant has a toxic effect on the body, secondary surgical operation(s) is usually unavoidable [7]. Stent applications used in cardiovascular surgery can condemn the patient to the use of blood thinners and similar drugs for life. Therefore, the use of biodegradable materials is

becoming more and more important for temporary and short-term treatments. Magnesium-based biomaterials are candidates for use as a new generation of biodegradable metals [7].

Although Mg-based biomaterials have biodegradable properties in in-body applications [8,9], they also contain some basic elements (Mg, Zn, Sn, Ca, etc.) needed by the body [10,11]. Moreover, the density and elasticity modulus values of pure Mg exhibit properties quite close to those of human bones [12]. However, the low corrosion resistance of pure Mg has shown that AZ61 [13,14], MgSnZn [13,15] new alloys and MgZnCa-(nHA reinforced) [16], Mg-(HA reinforced) [17], AZ31-(CNT reinforced) [18], and MgZrZn-(graphene nanoplatelet (GNP) reinforced) [19] biocomposites should be developed.

One of the most important factors affecting the corrosion resistance of Mg alloys is the intermetallic phases formed at the grain boundaries [15,20–22]. Depending on the increasing amount of intermetallic phase, different polarizations (anode and cathode) occur between the grain boundaries and the grain interiors. As a result of this situation, galvanic corrosion occurs [15,23,24]. Zn is one of the important alloying elements that increase the mechanical properties and corrosion resistance of Mg, and has biocompatible properties [15,25]. According to the Mg-Zn binary phase diagram [9,26], the solubility of the alloying element Zn in Mg is 6.2 wt.% at 325 °C [27], and at room temperature it is around 2 wt.%. During the rapid cooling to room temperature of the Mg alloy containing more than 2 wt.% Zn, intermetallic phase formation may start at the grain boundaries [26]. Therefore, it is expected that the rate of 2 wt.% should not be exceeded.

New Mg alloys with improved mechanical and corrosion properties have been produced by adding Al [28], Zn [29], Ca [30], Sn, and Mn [31] and various alloying elements to Mg [32]. However, for some applications, Mg alloys may still be insufficient. Therefore, studies on the production of Mg matrix composites have also gained momentum [10,30,33]. In the production of Mg matrix composites, two important issues should be considered in the selection of the reinforcement to be added. First, it must be biocompatible and have good corrosion resistance. Secondly, the mechanical strength of the reinforcement should be better than the matrix of the composite [13,30,34–36]. It is possible to say that ceramic reinforcement elements such as Al₂O₃, SiC, and HA (hydroxyapatite) can meet these requirements [9,13,37,38].

In some studies on MgMC, while the effect of the reinforcement addition on corrosion properties was investigated, Zn was generally used in the content of the matrix alloy [30,39,40]. Since the solubility of Zn in Mg at room temperature is maximum 2 wt.%, Mg₂Zn alloy was chosen as the matrix [39,41]. This is the reason why Mg₂Zn alloy was chosen as the matrix in the current study. The effect of Al₂O₃ reinforcement particles added at different proportions on hardness and corrosion properties was investigated. The paraffin coating technique facilitated the production of Mg-based materials with powder metallurgy. The hot pressing method (one of the PM methods) has been used as the production method to ensure the production of composite specimens with high relative densities, and to ensure a homogeneous distribution of reinforcement particles in the microstructure.

2. Materials and Methods

2.1. Mixing Process, Production, and Microstructural Investigation

The properties of the Mg and Zn powders used in the formation of the matrix alloy, and the chemical compositions of the Mg₂Zn alloy, are given in Table 1. The properties of Al₂O₃ powder used as reinforcement additions in different proportions and the chemical compositions of Mg₂Zn-x Al₂O₃ composites are given in Table 2. The powders used are of micron size and have high purity.

Table 1. The chemical composition and nomenclature of the matrix alloy.

Matrix Code	Matrix Nomenclature	Mg (wt.%) Purity: 99.8% Size: <45 μm	Zn (wt.%) Purity: 99.9% Size: <10 μm
X	Mg2Zn	98	2

Table 2. The chemical compositions and nomenclatures of the Mg2Zn-xAl₂O₃ composite specimens.

Composite Code	Composite Nomenclature	Mg2Zn (wt.%)	Al ₂ O ₃ (wt.%) Purity: 99.8% Size: <5 μm
X	Mg2Zn-0 wt.% Al ₂ O ₃	100	0
I	Mg2Zn-2 wt.% Al ₂ O ₃	98	2
II	Mg2Zn-4 wt.% Al ₂ O ₃	96	4
III	Mg2Zn-6 wt.% Al ₂ O ₃	94	6
IV	Mg2Zn-8 wt.% Al ₂ O ₃	92	8

During the weighing and mixing process of the powders, there is a risk of oxidation due to the contact of Mg powders with air. A paraffin coating technique was applied to the Mg powders to prevent this risk. Mg powders were supplied by the Alfa Aesar Company in a 500 g vacuum package. After the gross weight of the package was weighed, it was opened in a glove box and the Mg powders were poured into a beaker containing hexane. In determining the net weight of the Mg powders, the difference between the (gross) weight and the empty weight (tare) of the package was calculated. Precision scales (Precisia brand, Dietikon, Switzerland) with an accuracy of 10^{-4} g were used in the weighing processes. Before opening the package in the glove box, the cabin was filled with high purity argon gas and then vacuumed. The volume of the Mg powders was calculated by the ratio of its net weight to its density, and 20% by volume of paraffin was added to the hexane + Mg powders in the beaker (Figure 1a,b). The beaker containing the mixture was placed on a heater to completely dissolve the paraffin in hexane and was heated up to 70 °C (Figure 1c). While the beaker was on the heater, a propeller mixer was immersed into the mixture. Stirring was continued at 180 rpm for 60 min until all the hexane had evaporated. The same mixing procedures were repeated for the preparation of the mixtures specified in Tables 1 and 2. Important studies have been carried out to show that the mixing speed, time, and sintering temperature affect the microstructure, mechanical, and corrosion properties [42–44]. Therefore, in this study, mixing speed, time, and sintering parameters have been examined in previous studies [15,32,45], and the optimum production parameters were applied.

Specimens of each mixture were produced in a hot press bench using a graphite mold system of 30 mm length, 10 mm width, and 3.5 mm dimensions. The hot pressing system (Hidro Metal brand, Konya, Turkey) used in the study has a maximum temperature of 1000 °C and a capacity of 400 kN (Figure 1d). After 30 min of debinding at 300 °C, sintering processes were carried out using high purity argon gas at 625 °C under 50 MPa pressure for 60 min. Sanding, polishing, and etching processes were applied to the produced specimens, respectively. The solution of 5 vol.% nitric acid and 95 vol.% absolute ethyl alcohol, which is frequently used in the etching process of Mg based materials [46,47], was also used in the present study. SEM and EDS-mapping analyses were applied for the microstructure and phase examinations of the specimens. ImageJ software was used to measure average grain sizes of specimens. XRD analysis was carried out to determine phase formations of specimens before and after immersion tests. Measured densities of specimens were determined by following ASTM B962-14 [32,48]. According to this standard, also known as the Archimedes principle, the specimens were first weighed in air and then weighed in distilled water [32,48]. The theoretical density was calculated according to Equation (1).

The measured density/theoretical density ratio was used in the calculation of (%) relative density values.

$$\text{Theoretical density (g/cm}^3\text{)} = \frac{\text{Total mass}}{\text{Total volume}} = \frac{(\text{Mg mass}) + (\text{Zn mass}) + (\text{Al}_2\text{O}_3 \text{ mass})}{\left[\frac{\text{Mg mass}}{\text{Mg density}}\right] + \left[\frac{\text{Zn mass}}{\text{Zn density}}\right] + \left[\frac{\text{Al}_2\text{O}_3 \text{ mass}}{\text{Al}_2\text{O}_3 \text{ density}}\right]} \quad (1)$$

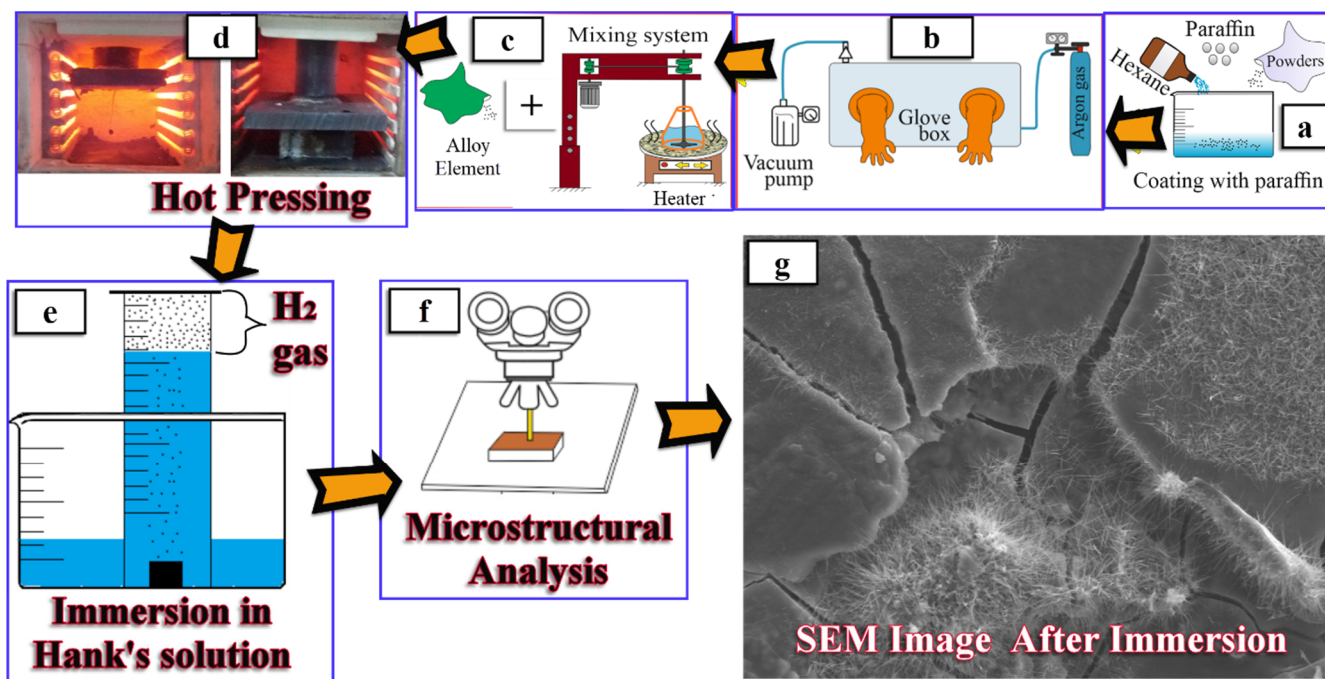


Figure 1. Graphical presentation of (a) paraffin coating of powders, (b) glove box system, (c) adding alloying elements, (d) hot pressing, (e) measuring evolved H₂ gas, (f) microstructural analysis, (g) a SEM image after immersion process.

2.2. Mechanical and Corrosion Test

Hardness tests were applied for 15 s with 300 g load, to determine the mechanical properties of the specimens. A micro Vickers hardness tester (AOB Labtt brand, İstanbul, Turkey) was used to obtain the hardness values. The average of the measurements taken from five different regions of each specimen was accepted as the hardness value. A shimadzu tensile test device with a capacity of 10 kN was used for tensile tests in air at room temperature. Pull rate was chosen as 0.5 mm/min. Rectangular prism-shaped specimens (30 × 10 × 3 mm) were cut with wire. The produced specimens were formed into tensile specimens according to the MPIF-10 standard.

Corrosion tests were carried out according to standards reported in the literature [15,28,49]. Weight loss (%) and evolved H₂ gas measurements were considered in determining the corrosion behavior of Mg₂Zn-xAl₂O₃ specimens. In the tests, specimens were subjected to sanding and polishing in 10 × 10 × 3 mm (length × width × height) dimensions and Hank's solution [15] were used as the corrosion fluid. The ratio of corrosion liquid to total surface area of specimen was applied as 20:1 (mL/cm²). When the specimens were placed in the corrosion liquid in the beaker, a graduated measure, where the evolved H₂ gas could accumulate, was placed on the specimen. The specified system was used for 10 days in an incubator at 37 °C constant temperature (Figure 1e). The corrosion fluid was renewed every 12 h, and the H₂ gas accumulated in the cylinder was measured. When the specimens were taken from the corrosion liquid, they were firstly cleaned with pure ethyl alcohol and then placed in a desiccator to dry. After the drying process was applied to the specimens, their weight was measured. The specimen weight loss (%) was

calculated according to Equation (2). After the 10-day corrosion process was completed, the specimen's surface structure was examined with SEM and EDS (Figure 1f,g).

$$\text{Weight loss accuracy (\%)} = \frac{(\text{Last weight} - \text{First weight}) \text{ of specimen}}{\text{First weight of specimen}} \times 100 \quad (2)$$

3. Results and Discussions

The changes of theoretical density, measured density, and relative density data, depending on the increasing reinforcement ratio, are given in Figure 2. The theoretical and measured density values increase with increasing reinforcement ratio. However, the relative density values of specimens with high reinforcement additions are lower than the other specimens. It has been frequently stated in the literature that the sintering process is successfully performed when the relative density values of the materials produced by powder metallurgy method are above 95% [17,43]. In the present study, even the lowest relative density value was higher than 98%, indicating that the Mg₂Zn-xAl₂O₃ composite specimens were successfully produced by the hot pressing method.

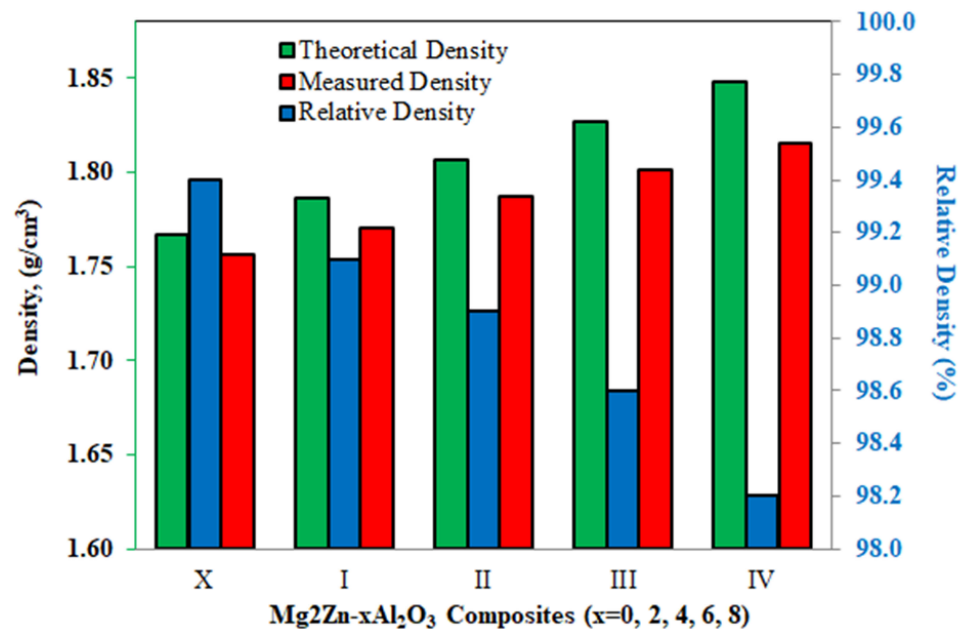


Figure 2. Theoretical, measured, and relative density values of Mg₂Zn-x Al₂O₃ composite specimens.

3.1. SEM and EDS Analysis of Specimens before Immersion

The EDS-mapping analysis images of the specimens containing 2 wt.% Al₂O₃ and 8 wt.% Al₂O₃ are given in Figure 3a,b, respectively. The regions (inside matrix) which have a rich Mg content are shown in a green color. The Mg content is more intense in the grains. The Zn content can be seen in every region (pink color). If the mapped distributions of Mg, Al, and O elements are examined together, the Mg content in the grain boundary regions is almost nonexistent (black color), while the contents of Al (blue color) and O (red color) are much richer in the same regions. According to this result, it is understood that the white structures in the grain boundaries belong to the Al₂O₃ reinforcement particles.

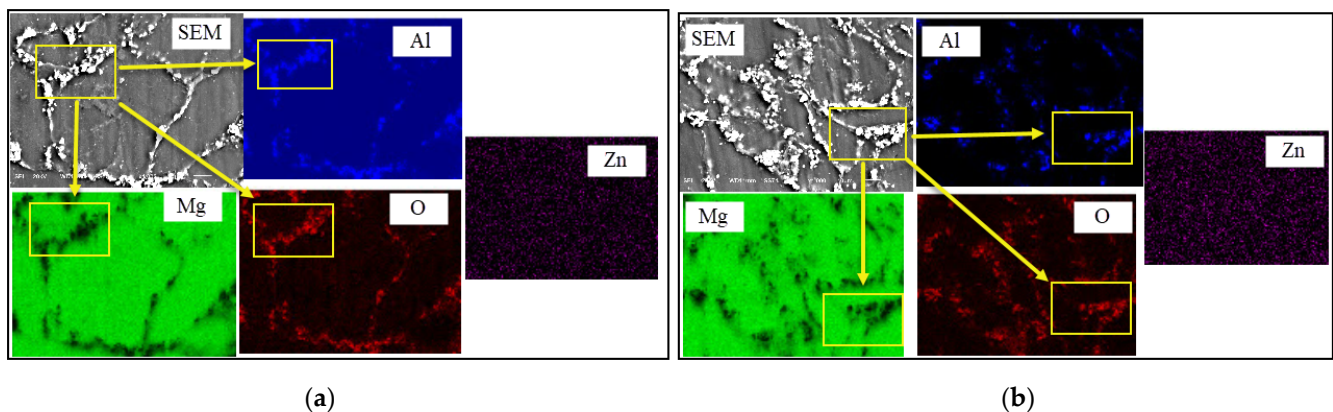


Figure 3. SEM/EDS mapping analysis before immersion (a) Mg₂Zn-2 wt.% Al₂O₃ magnesium composite, (b) Mg₂Zn-8 wt.% Al₂O₃ magnesium composite.

SEM images of Mg₂Zn-*x*Al₂O₃ composite specimens are given in Figure 4. Grains and grain boundaries can be clearly seen in all the sintered specimens. From the SEM images, it can be seen that all the specimens have a very dense microstructure. Additionally, no pore structures were found in the microstructure. The microstructural images also support the relative density graphs in Figure 2. Al₂O₃ particles are homogeneously distributed in the grain boundaries of the Al₂O₃ reinforced specimens. It was also observed that there is no clustering of reinforcing particles in any region. It has been determined that the production method (PM method) is considerably effective in obtaining a homogeneous microstructure, both in the present study and in other literature studies [10,47,50]. With the increasing rate of reinforcement, the amount of Al₂O₃ particles at the grain boundaries increases and the grain sizes are generally smaller. It is thought that specimens with higher content of Al₂O₃ have finer-grained microstructures, as the reinforcement particles act as barriers. Average grain sizes of the specimens X, I, II, III, and IV are 34.82 μm, 29.96 μm, 29.21 μm, 23.72 μm, and 18.75 μm, respectively. For similar studies reported in the literature, it was determined that grain growth was prevented due to the increasing rate of hard structures homogeneously distributed at the grain boundaries [47,51,52].

The SEM images also show that all specimens achieved a good degree of wettability. As a wettability criterion, there is no pore at the contact points of the reinforcement particles and the Mg matrix. The use of Mg alloy as a matrix is effective in the high wettability of the specimens. In a different study, Suresh et al. [53] found that Mg increases the wettability properties of composite materials.

After the Mg₂Zn-*x*Al₂O₃ composite specimens were produced through hot pressing method, XRD analysis was applied to all specimens to determine phases in the microstructure. Figure 5 shows the XRD patterns of specimens before immersion test. First of all, when the XRD patterns of the Mg₂Zn alloy without alumina reinforcement were examined, no oxygen-containing phase was found. While the peaks of the Mg phase were obtained in all specimens, the peaks of the Al₂O₃ phase could be seen more clearly with the increasing alumina reinforcement. The solubility of Zn alloying element in Mg at room temperature is about 2 wt.%. Therefore, the inability to obtain any peak of the Zn alloy element in the matrix in the XRD analysis was attributed to this situation. In similar literature studies [15,31,54], no peak could be detected in XRD analyses when the Zn content added to magnesium was less than 4 wt.%.

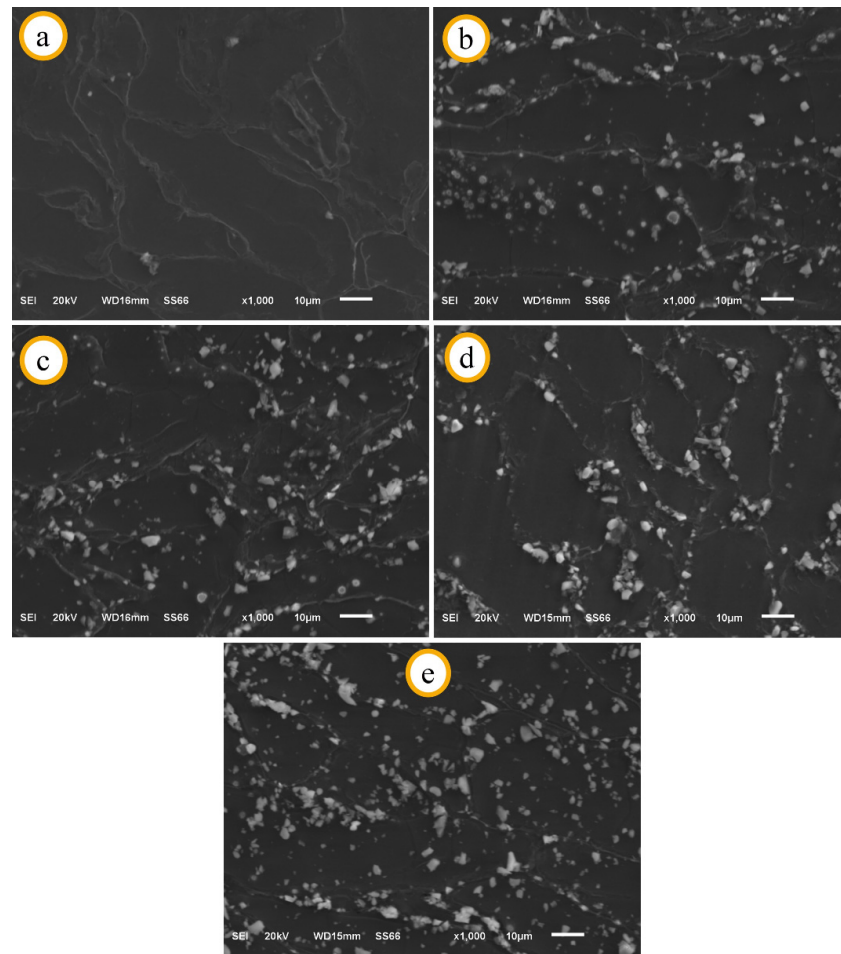


Figure 4. SEM images (at 1000 \times magnification) of Al_2O_3 reinforced Mg_2Zn matrix magnesium composites before immersion: (a) X, (b) I, (c) II, (d) III, (e) IV.

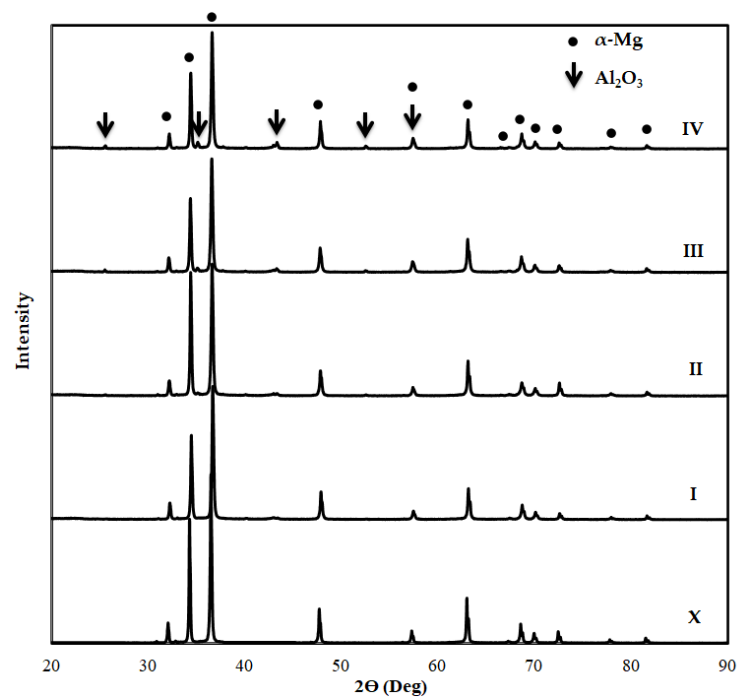


Figure 5. XRD patterns of Al_2O_3 reinforced Mg_2Zn matrix magnesium composites before immersion.

3.2. Corrosion Properties of Mg₂Zn-xAl₂O₃ Composites

SEM images taken from the surfaces of the specimens (X, I, II, and III) after 10 days of immersion are given in Figure 6. The specimen (IV), containing 8 wt.% Al₂O₃, was exposed to degradation due to excessive corrosion at the end of the 10-day immersion period, and the SEM image of this specimen could not be taken. It can be seen that the surface structures of the specimens X and I are in good condition (Figure 6a,b), and large pitting corrosion has occurred on the surfaces of the specimens (II) and (III) (Figure 6c,d). The pits on the surface of specimen (III) are greater and larger than those on the surface of specimen (II). In the pre-corrosion SEM examination of the specimens, when the reinforcement addition was more than 2 wt.%, the amount of Al₂O₃ particles at the grain boundaries increased. It is thought that the grain interior (anode) and grain boundaries (cathode) behave as different poles during corrosion [23,24], and pits on the surface (Figure 6c,d) are formed as a result of galvanic corrosion. On the surface of the Mg₂Zn matrix alloy (Figure 6a), it can be seen that different layer structures are formed in some regions, and the layer formed in certain regions is detached from the surface. Moreover, there are many and very long cracks on the surface. No pitting corrosion occurred on the surface of the specimen (I) with dense white structures being detected on the surface (Figure 6b).

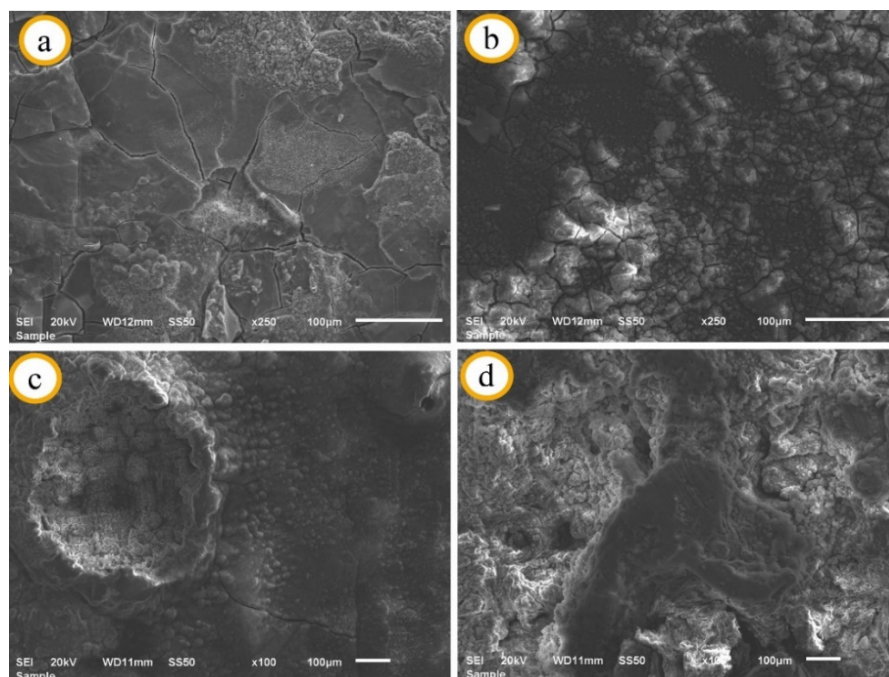
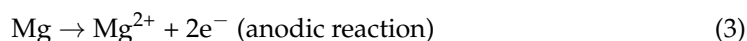


Figure 6. SEM images after immersion; (a) X, (b) I, (c) II, (d) III.

During the corrosion of Mg in Hank's solution, the reactions in Equations (3)–(6) occur [54–56]. According to Equation (5), the higher the formation of Mg(OH)₂ corrosion product on the specimen surface, the higher the H₂ gas volume evolved at the same rate.



EDS analysis, elemental peaks and contents of specimens (X, I, and II) are given in Figure 7. In Figure 7a, the structures indicated with green circles are very rich in Mg and O content. Therefore, it is thought that the $\text{Mg}(\text{OH})_2$ layer was newly formed in the specified green areas. The $\text{Mg}(\text{OH})_2$ film, which forms as layers on the surface after a certain period of time, is broken by the effect of the continuously evolved H_2 gas. When the cracks where H_2 gas is evolved are deeper and wider, the protective layer between the cracks can break off the surface (orange-colored circle). The surface under the separated layer comes into contact with the corrosion fluid and the corrosion reaction cycle continues. As the number of repetitions of this cycle increases, pitting corrosion occurs as seen in the SEM images in Figure 6c,d. When the temporary $\text{Mg}(\text{OH})_2$ film layer formed on the specimen surface remains for a longer period without leaving the surface, it is expected to react according to Equation (7) [15,55]. After this reaction, the reaction in Equation (8) is also expected to occur, and permanent and protective apatite structures are formed on the surface [10]. When the Figure 7b was examined, it was determined by EDS elemental analysis that the reactions stated in Equations (7) and (8) took place mostly on the surface of the specimen (I) containing 2 wt.% Al_2O_3 . The region indicated on the SEM image with the turquoise-colored rectangle is very rich in terms of Mg, Ca, P, and O contents. It was determined that the layers indicated with a turquoise arrow and rectangle belong to the apatite structures. Apatite structures fill the cracks where H_2 gas is evolved and serve as a kind of coating on the specimen surface. According to the findings reported in the literature [10,15], the apatite structures significantly improve the corrosion resistance. In the present study, it is thought that the corrosion properties of the specimen (I) with apatite structure are better. In Figure 7c, it is thought that the loose products were separated from the surface in a short time period and this period was completed before the $\text{Mg}(\text{OH})_2$ layer on the products could not transform into apatite structures. Detection of low content of Ca and P on the surface is associated with this situation according to EDS analysis of surface in Figure 7c.



Figure 8 shows the XRD analysis of Al_2O_3 reinforced Mg2Zn matrix magnesium composites after immersion. The peaks at $2\theta = 19.16^\circ$, 38.30° , 51.05° , 58.94° , and 62.32° show the $\text{Mg}(\text{OH})_2$ phases. Mg peaks are obtained at $2\theta = 32.58^\circ$, 34.72° , 37.02° , 48.26° , 57.90° , 63.48° , 68.98° , 70.36° , and 72.86° . The obtained findings are compatible with the literature studies [57,58]. The $\text{Mg}(\text{OH})_2$ phase ratio is high on specimen surfaces containing high Al_2O_3 reinforcement. On the other hand, the Mg phase ratio is at low levels. Mg phases decrease with the increase of $\text{Mg}(\text{OH})_2$ phases. This indicates that a large amount of Mg is converted to $\text{Mg}(\text{OH})_2$ formation on the surface. HA peaks can be clearly seen in the XRD patterns of specimen (I) at $2\theta = 12.24^\circ$, 28.40° , and 33.38° . The fact that the HA ($\text{Ca}_{10}(\text{PO}_4)_6(\text{OH})_2$) phases are more prominent in the specimen (I) is based on the corrosion inhibition property of the added Al_2O_3 reinforcement at low content (2 wt.%). It is known that the anode and cathode polarization increases with the increasing alumina reinforcement ratio and the desired resistance to galvanic corrosion cannot be demonstrated [57,59]. Therefore, in SEM images after immersion, pitting corrosion was observed in specimens containing high Al_2O_3 . Pitting corrosion was not observed due to the formation of HA structure on the surface of the specimens containing 2 wt.% Al_2O_3 .

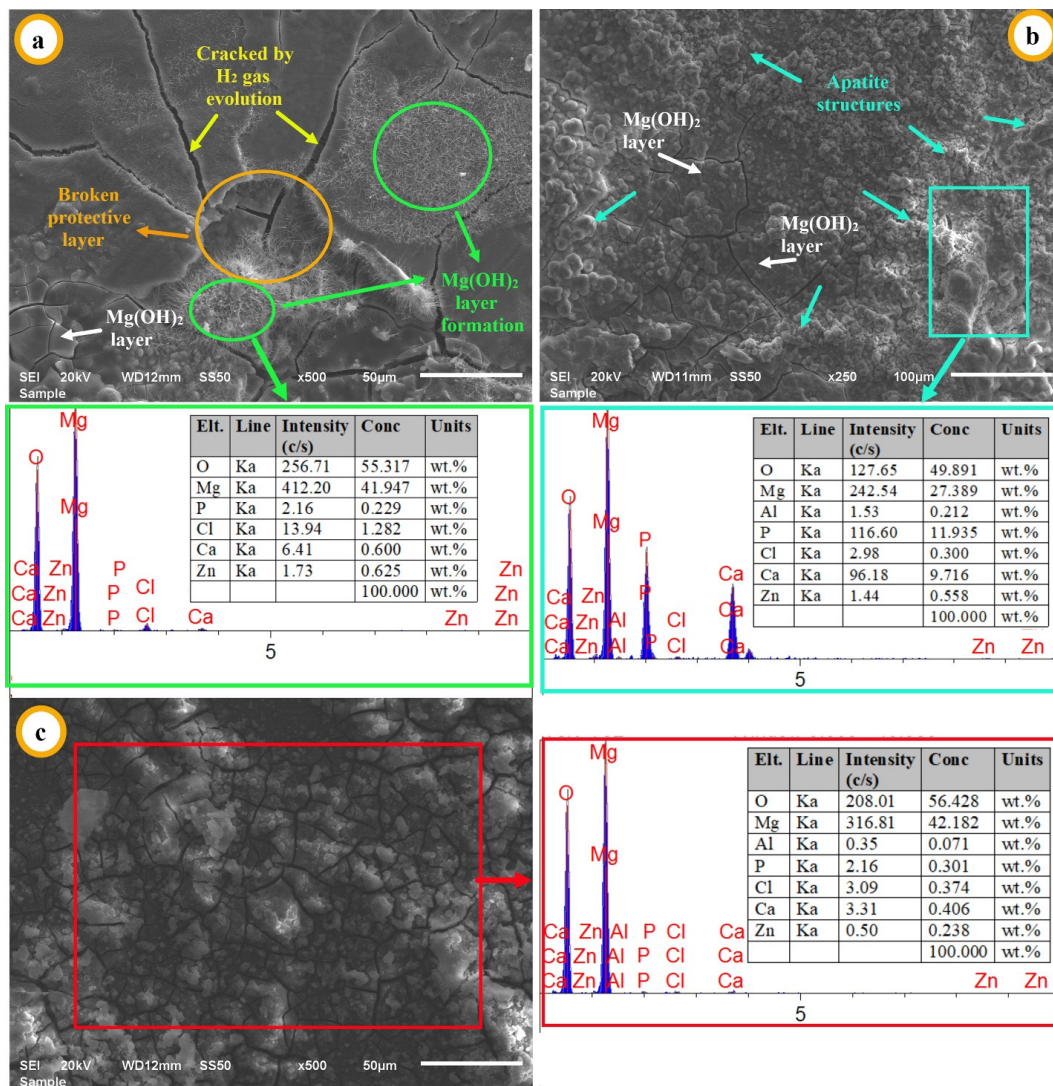


Figure 7. EDS analysis after immersion: (a) X, (b) I, (c) II.

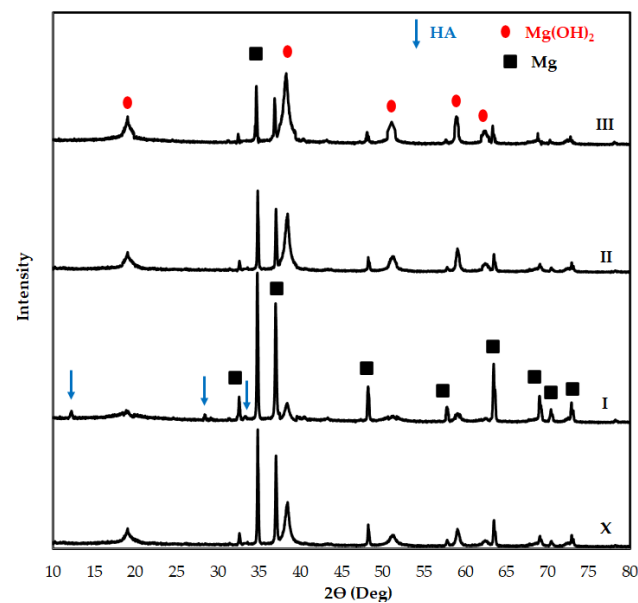


Figure 8. XRD patterns of Al₂O₃ reinforced Mg₂Zn matrix magnesium composites after immersion.

It is well known that Al_2O_3 has a good corrosion resistance. While corrosion resistance is expected to increase with increasing Al_2O_3 reinforcement ratio, corrosion resistance decreased in specimens containing more than 2 wt.% Al_2O_3 reinforcement. This is attributed to the formation of sufficient time period for the $\text{Mg}(\text{OH})_2$ structures that are constantly present on the surface to transform into HA structures. As stated earlier in the SEM/EDS mapping analysis, Al_2O_3 particles are observed to be more dense at the grain boundaries with increasing Al_2O_3 reinforcement ratio. This increases the interface between matrix and reinforcement. It is reported that reduction of galvanic corrosion between grain boundary and matrix enhanced corrosion resistance [60]. Therefore, in the present study, high activity of the galvanic corrosion occurred in specimens containing high Al_2O_3 reinforcement. It is also thought that there is not enough activity of galvanic corrosion to reduce the time period required for the formation of apatite structures on the surface of the specimen containing 2 wt.% Al_2O_3 . It is reported in a similar study [61] that the increase of reinforcement ratio in the magnesium matrix composites causes high activity of the galvanic corrosion.

After the immersion process was applied for 10 days, the daily (%) weight loss of the specimens and the evolved H_2 gas values are given in Figure 9. With the increase in the immersion time, both the weight loss and the amount of evolved H_2 gas increase. While the corrosion rate increased continuously in all specimens, the corrosion rate of the 2 wt.% Al_2O_3 reinforced composite specimen stopped growing from the 7th day. The best corrosion properties were also obtained from this specimen. With the addition of more reinforcement than this ratio, the corrosion properties were negatively affected. The reason why this specimen exhibits better corrosion behavior compared to other specimens is the apatite structures whose presence on the surface was detected in SEM-EDS examinations. In specimens with high reinforcement ratios, it is thought that the dense reinforcement particles at grain boundaries trigger galvanic corrosion and negatively affect the corrosion resistance.

Another notable observation in Figure 9 is that a small amount of H_2 gas is evolved from the specimen with low weight loss and the amount of evolved H_2 gas increases as the weight loss rate increases. When Equation (4) and XRD analysis after immersion are examined together, the amount of evolved H_2 gas is directly associated with the formation of $\text{Mg}(\text{OH})_2$ layer on the surface. The pitting corrosion causes on the surface during immersion means that the interface between the specimen and the corrosion liquid increases. This means more $\text{Mg}(\text{OH})_2$ formation and more evolved H_2 gas. Therefore, the amount of evolved H_2 gas also increases with the increase in weight loss ratio (Figure 9). In a study on corrosion of MgMC [17], HA in different proportions was added to the Mg3Zn matrix and the composite was subjected to an immersion process. The composite specimen with the addition of 5 wt.% HA, for which they achieved the best results, lost about 27% weight. In the present study, the lowest weight loss was obtained from the specimen containing 2 wt.% Al_2O_3 at approximately 9%. This value is 18% less than the result obtained by Dubey et al. In a different study, Jayalakshmi et al. [20] examined the corrosion properties of AM100 and ZC63 magnesium alloys by adding different amounts of saffil alumina short fiber reinforcement by volume. They obtained the best corrosion properties at approximately 7 mm/year, and approximately 9.5 mm/year from AM100 + 25 vol.% alumina and ZC63 + 25 vol.% alumina specimens, respectively. In the present study, a weight loss of 9% corresponds to approximately 2.5 mm/year when converted to the unit system mm/year. This value is 280% less than AM100 + 25 vol.% alumina and 380% less than ZC63 + 25 vol.% alumina. A comparative presentation of the corrosion properties obtained in present study with some literature studies is given in Table 3.

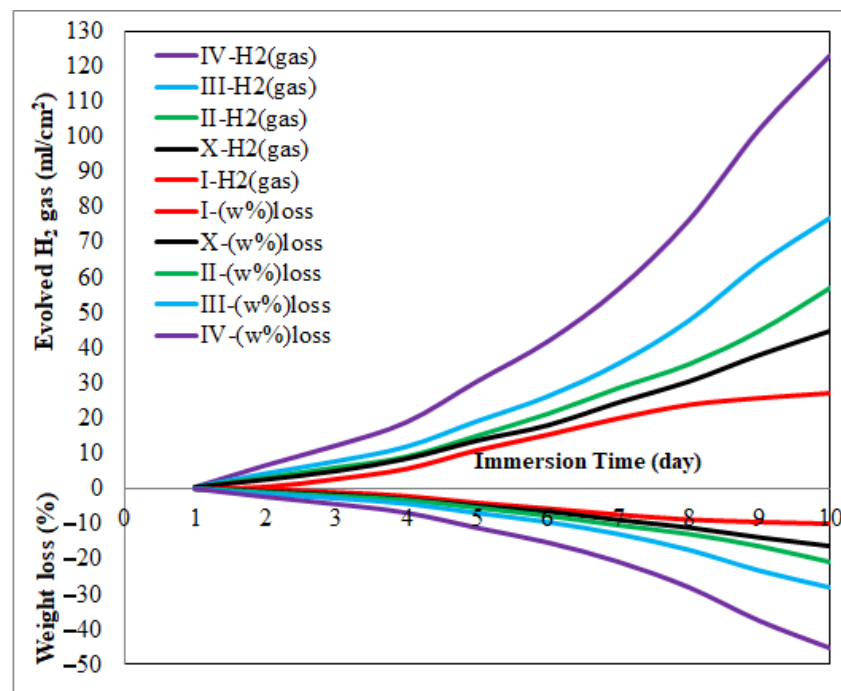


Figure 9. Weight loss (%) and evolved H₂ gas (ml/cm²) after 10 days of immersion.

Table 3. A comparative presentation of the corrosion properties obtained in present study with some literature studies.

Material	Corrosion Rate (mm/Year)	Weight Loss (%)	Ref
Mg2Zn + 2 wt.% Al ₂ O ₃	2.5	9	PS
AM100 + 25 vol.% Al ₂ O ₃	7	-	[20]
ZC63 + 25 vol.% Al ₂ O ₃	9.5	-	[20]
Mg3Zn + 5HA	-	27	[17]
Mg0.3GNP	4	-	[57]
Mg0.5Zr0.5GNP	18	-	[19]

PS: Present study. GNP: graphene nanoplatelet.

3.3. Mechanical Properties of Mg₂Zn-xAl₂O₃ Composite Specimens

Figure 10 shows the hardness values of Mg₂Zn-xAl₂O₃ composite specimens. When the graph is examined, it can be seen that particle reinforcement has a positive effect on the hardness properties. It is thought that the increase in hardness occurs due to two reasons. The first is that the particle reinforcements, which are harder than the grain interiors (Mg₂Zn matrix), have a reticulated structure at the grain boundaries. The other is that finer-grained structures were obtained due to Al₂O₃ particles acting as barriers at grain boundaries. Kandemir et al. [33] used AZ91 magnesium alloy, which is widely used in the industry, as a matrix and added up to 0.5 wt.% GNP. The highest hardness value from their composites was 69 HV. In a study by Lotfpour et al. using the same matrix alloy [41], they added Cu in different proportions to the Mg₂Zn matrix. They obtained a highest hardness value of approximately 78 HB from the material with 5 wt.% Cu added. This value corresponds to a hardness value of about 82 HV. In the present study, the hardness value is 30% higher than the value obtained by Kandemir et al. [33], and 10% higher than the result obtained by Lotfpour et al. [41].

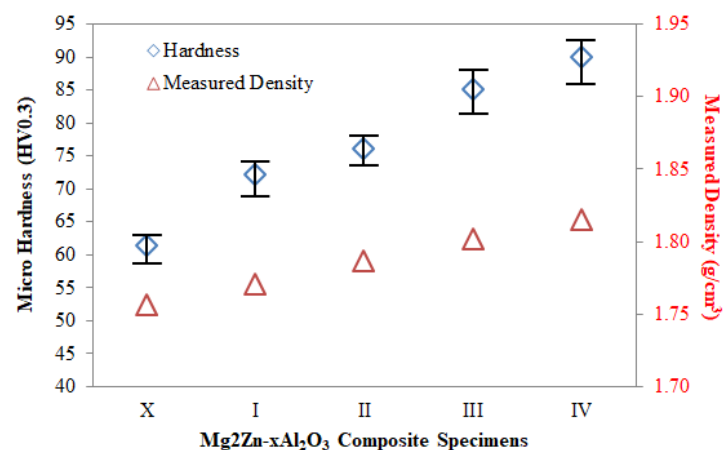


Figure 10. The micro hardness values of Mg2Zn-xAl₂O₃ composite specimens.

Figure 11 shows the tensile strength-elongation (%) curves of Mg2Zn-xAl₂O₃ composite specimens. It is seen that the tensile strength, yield strength, and elongation values of Al₂O₃ reinforced composites increased compared to Mg2Zn alloy. Depending on the increasing Al₂O₃ reinforcement ratio, the tensile strength increased steadily. Elongation (%) increases when Al₂O₃ reinforcement up to 4% by weight is added. However, elongation (%) decreases with the addition of more Al₂O₃ than this ratio. This result is in agreement with the investigation reported in literature [62,63]. The tensile strength of the Al₂O₃ reinforced specimens increases because of the addition of hard alumina particles in a softer matrix. In addition, fine-grained structures are thought to be effective in the development of tensile strength of specimens. It has also been stated in previous studies [31,47] that hard structures, which are densely located at the grain boundaries, act as barriers and make dislocation movements difficult. According to the literature [64], it may be also attributable to synergetic strengthening mechanisms including difference in elastic modulus strengthening, load-transfer strengthening, and difference in thermal expansion strengthening. Significant improvements in tensile strengths are observed in alumina particulate reinforced specimens in comparison composites Mg3Zn-5HA [17], AZ91-0.5 GNP [33], and Mg2Zn-5Cu [41]. The highest tensile strength value of approximately 191 MPa was from the specimen with 8 wt.% Al₂O₃. Considering the best corrosion results in the present study, the tensile strength of the specimen containing 2% alumina was approximately 160 MPa. This value is 26% higher than tensile strengths of Mg2Zn in present study, 11% higher than AZ91 [33], 19% higher than Mg2Zn-5Cu [41], and 33% higher than AZ91-2 wt.% SiC [17], respectively. A comparative presentation of the mechanical properties obtained in present study with some literature studies is given in Table 4.

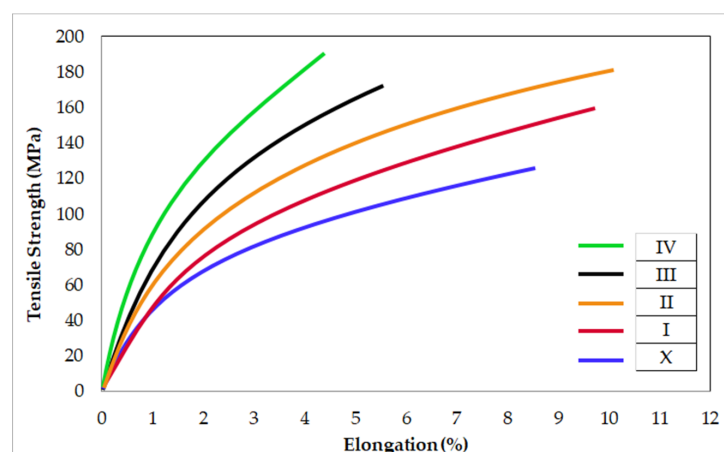


Figure 11. The tensile strength-elongation (%) curves of Mg2Zn-xAl₂O₃ composite specimens.

Table 4. A comparative presentation of the mechanical properties obtained in present study with some literature studies.

Material	Hardness (HV)	Tensile Strength (MPa)	Elongation (%)	Ref
Mg2Zn-2 wt.% Al ₂ O ₃	72.2	160	9.8	PS
Mg2Zn-8 wt.% Al ₂ O ₃	89.9	191	4.4	PS
AZ91-2 wt.% SiC	75	120	4	[62]
AZ91-8 wt.% SiC	85	145	3.5	[62]
Mg/Mg2Si-HO		145		[65]
Mg/Mg2Si-HR		155		[65]
Mg0.5Zr0.5GNP	53	-	-	[19]
Mg3Zn-0.5Cu	62	171	15	[41]
Mg3Zn-5Cu	80	135	6	[41]
AZ91-0.5 wt.% GNP	69	-	-	[33]

PS: Present study.

4. Conclusions

In the present study, Al₂O₃ reinforced Mg2Zn matrix magnesium composites were successfully produced through the hot pressing method. The hardness and corrosion properties were investigated experimentally. The results of the analyses are as follows:

The risk of exposure of Mg powders to oxidation from the mixing process to the sintering stage has been eliminated due to the paraffin coating technique. MgMCs were produced with high relative density ratios by the hot pressing method.

The added Al₂O₃ particle reinforcements were homogeneously distributed at the grain boundaries and they were effective in grain refinement. Alumina reinforcement significantly improved the mechanical properties. Maximum hardness and tensile strength were obtained from the specimen containing 8 wt.% Al₂O₃ reinforcement. In the specimens where the alumina reinforcement ratio increased up to 4 wt.%, an increase in the % elongation values was achieved and the highest value was obtained from this specimen.

After immersion, Mg(OH)₂ and the apatite structures were generally determined on the specimen surfaces. Apatite structures were densely formed on the surface of specimen (I) only. Apatite structures exhibited a permanent and protective behavior, resulting in a significant reduction in the corrosion rate and the amount of evolved H₂ gas. Corrosion resistance is significantly reduced in specimens containing a high reinforcement ratio. As the corrosion resistance decreased, the amount of evolved H₂ gas increased. When Al₂O₃ reinforcement is added at a low ratio (2 wt.%), galvanic corrosion is the minimum at the grain boundaries. This allows the formation of the apatite structure which improves the corrosion properties of the magnesium matrix composite material.

Paraffin coating technique enabled the production of other Mg-based alloys and composites by powder metallurgy method. By using the hot pressing method, there will be no need for an additional production process and this will help the development of the microstructure of different Mg-based materials. In applications where the mechanical and corrosion resistance of Mg based composites are required together, it is recommended to add 2 wt.% Al₂O₃ to the relevant composite content.

Author Contributions: Conceptualization, A.E.; methodology, A.E.; investigation, A.E. and D.Y.P.; resources, A.E.; writing—review and editing, A.E. and D.Y.P.; visualization, A.E.; funding acquisition, D.Y.P. All authors have read and agreed to the published version of the manuscript.

Funding: This research received no external funding.

Data Availability Statement: All data generated or analyzed during this study are included in this article.

Acknowledgments: The authors would like to thank Bingol University, Central Research Laboratory of Bingol University (exertion in SEM, EDS and XRD analysis), and Afyon Kocatepe University (exertion in tensile tests).

Conflicts of Interest: The authors declare no conflict of interest.

References

1. Suresh Kumar, N.; Padma Suvarna, R.; Chandra Babu Naidu, K.; Banerjee, P.; Ratnamala, A.; Manjunatha, H. A review on biological and biomimetic materials and their applications. *Appl. Phys. A Mater. Sci. Process.* **2020**, *126*, 1–18. [[CrossRef](#)]
2. Shadanbaz, S.; Dias, G.J. Calcium phosphate coatings on magnesium alloys for biomedical applications: A review. *Acta Biomater.* **2012**, *8*, 20–30. [[CrossRef](#)]
3. Shanmugam, L.; Kazemi, M.E.; Qiu, C.; Rui, M.; Yang, L.; Yang, J. Influence of UHMWPE fiber and Ti6Al4V metal surface treatments on the low-velocity impact behavior of thermoplastic fiber metal laminates. *Adv. Compos. Hybrid Mater.* **2020**, *3*, 508–521. [[CrossRef](#)]
4. Johnston, S.; Shi, Z.; Venezuela, J.; Wen, C.; Dargusch, M.S.; Atrens, A. Investigating Mg biocorrosion in vitro: Lessons learned and recommendations. *JOM* **2019**, *71*, 1406–1413. [[CrossRef](#)]
5. Castellani, C.; Lindtner, R.A.; Hausbrandt, P.; Tschegg, E.; Stanzl-Tschegg, S.E.; Zanoni, G.; Beck, S.; Weinberg, A.M. Bone-implant interface strength and osseointegration: Biodegradable magnesium alloy versus standard titanium control. *Acta Biomater.* **2011**, *7*, 432–440. [[CrossRef](#)]
6. Yun, Y.H.; Dong, Z.; Yang, D.; Schulz, M.J.; Shanov, V.N.; Yarmolenko, S.; Xu, Z.; Kumta, P.; Sfeir, C. Biodegradable Mg corrosion and osteoblast cell culture studies. *Mater. Sci. Eng. C* **2009**, *29*, 1814–1821. [[CrossRef](#)]
7. Sezer, N.; Evis, Z.; Kayhan, S.M.; Tahmasebifar, A.; Koç, M. Review of magnesium-based biomaterials and their applications. *J. Magnes. Alloy* **2018**, *6*, 23–43. [[CrossRef](#)]
8. Aljihmani, L.; Alic, L.; Boudjemline, Y.; Hijazi, Z.M.; Mansoor, B.; Serpedin, E.; Qaraqe, K. Magnesium-based bioresorbable stent materials: Review of reviews. *J. Bio-Tribo-Corros.* **2019**, *5*, 26. [[CrossRef](#)]
9. Mahapatro, A.; Arshanapalli, S.A. Bioceramic coatings on magnesium alloys. *J. Bio-Tribo-Corros.* **2017**, *3*, 1–9. [[CrossRef](#)]
10. Mokhtari, S.; Eftekhari Yekta, B.; Marghussian, V.; Ahmadi, P.T. Synthesis and characterization of biodegradable AZ31/calcium phosphate glass composites for orthopedic applications. *Adv. Compos. Hybrid Mater.* **2020**, *3*, 390–401. [[CrossRef](#)]
11. Li, X.; Liu, X.; Wu, S.; Yeung, K.W.K.; Zheng, Y.; Chu, P.K. Design of magnesium alloys with controllable degradation for biomedical implants: From bulk to surface. *Acta Biomater.* **2016**, *45*, 2–30. [[CrossRef](#)]
12. Xin, Y.; Hu, T.; Chu, P.K. In vitro studies of biomedical magnesium alloys in a simulated physiological environment: A review. *Acta Biomater.* **2011**, *7*, 1452–1459. [[CrossRef](#)]
13. Liu, W.; Wang, X.; Hu, X.; Wu, K.; Zheng, M. Effects of hot rolling on microstructure, macrotexture and mechanical properties of pre-extruded AZ31/SiC nanocomposite sheets. *Mater. Sci. Eng. A* **2017**, *683*, 15–23. [[CrossRef](#)]
14. Abbas, A.T.; Pimenov, D.Y.; Erdakov, I.N.; Taha, M.A.; Soliman, M.S.; El Rayes, M.M. ANN surface roughness optimization of AZ61 magnesium alloy finish turning: Minimum machining times at prime machining costs. *Materials* **2018**, *11*, 808. [[CrossRef](#)]
15. Erceetin, A.; Özgün, Ö.; Aslantas, K.; Aykutoğlu, G. The microstructure, degradation behavior and cytotoxicity effect of Mg–Sn–Zn alloys in vitro tests. *SN Appl. Sci.* **2020**, *2*, 173. [[CrossRef](#)]
16. Aboudzadeh, N.; Dehghanian, C.; Shokrgozar, M.A. Synthesis, microstructure and mechanical properties of Mg–5Zn–0.3Ca/nHA nanocomposites. *Iran. J. Mater. Sci. Eng.* **2017**, *14*, 58–68. [[CrossRef](#)]
17. Dubey, A.; Jaiswal, S.; Lahiri, D. Mechanical integrity of biodegradable Mg–HA composite during in vitro exposure. *J. Mater. Eng. Perform.* **2019**, *28*, 800–809. [[CrossRef](#)]
18. Kumar, A.M.; Hassan, S.F.; Sorour, A.A.; Paramsothy, M.; Gupta, M. Investigation on the controlled degradation and invitro mineralization of carbon nanotube reinforced AZ31 nanocomposite in simulated body fluid. *Met. Mater. Int.* **2019**, *25*, 105–116. [[CrossRef](#)]
19. Shahin, M.; Wen, C.; Munir, K.; Li, Y. Mechanical and corrosion properties of graphene nanoplatelet–reinforced Mg–Zr and Mg–Zr–Zn matrix nanocomposites for biomedical applications. *J. Magnes. Alloy* **2021**. [[CrossRef](#)]
20. Jayalakshmi, S.; Singh, R.A.; Chen, X.; Konovalov, S.; Srivatsan, T.S.; Seshan, S.; Gupta, M. Role of matrix microstructure in governing the mechanical behavior and corrosion response of two magnesium alloy metal matrix composites. *JOM* **2020**, *72*, 2882–2891. [[CrossRef](#)]
21. Gu, X.; Cheng, W.; Cheng, S.; Liu, Y.; Wang, Z.; Yu, H.; Cui, Z.; Wang, L.; Wang, H. Tailoring the microstructure and improving the discharge properties of dilute Mg–Sn–Mn–Ca alloy as anode for Mg–air battery through homogenization prior to extrusion. *J. Mater. Sci. Technol.* **2021**, *60*, 77–89. [[CrossRef](#)]
22. Yan, Y.; Liu, X.; Xiong, H.; Zhou, J.; Yu, H.; Qin, C.; Wang, Z. Stearic acid coated MgO nanoplate arrays as effective hydrophobic films for improving corrosion resistance of Mg-based metallic glasses. *Nanomaterials* **2020**, *10*, 947. [[CrossRef](#)] [[PubMed](#)]
23. Zeng, R.C.; Zhang, J.; Huang, W.J.; Dietzel, W.; Kainer, K.U.; Blawert, C.; Ke, W. Review of studies on corrosion of magnesium alloys. *Trans. Nonferrous Met. Soc. China Engl. Ed.* **2006**, *16*, s763–s771. [[CrossRef](#)]
24. Cai, S.; Lei, T.; Li, N.; Feng, F. Effects of Zn on microstructure, mechanical properties and corrosion behavior of Mg–Zn alloys. *Mater. Sci. Eng. C* **2012**, *32*, 2570–2577. [[CrossRef](#)]
25. Li, H.; Zheng, Y.; Qin, L. Progress of biodegradable metals. *Prog. Nat. Sci. Mater. Int.* **2014**, *24*, 414–422. [[CrossRef](#)]
26. Kevorkov, D.; Pekguleryuz, M. Experimental study of the Ce–Mg–Zn phase diagram at 350 °C via diffusion couple techniques. *J. Alloys Compd.* **2009**, *478*, 427–436. [[CrossRef](#)]

27. Ramesh, S.; Anne, G.; Nayaka, H.S.; Sahu, S.; Ramesh, M.R. Influence of multidirectional forging on microstructural, mechanical, and corrosion behavior of Mg-Zn alloy. *J. Mater. Eng. Perform.* **2019**, *28*, 2053–2062. [[CrossRef](#)]
28. Wu, W.; Zhang, F.; Li, Y.; Song, L.; Jiang, D.; Zeng, R.C.; Tjong, S.C.; Chen, D.C. Corrosion resistance of dodecanethiol-modified magnesium hydroxide coating on AZ31 magnesium alloy. *Appl. Phys. A Mater. Sci. Process.* **2020**, *126*, 1–11. [[CrossRef](#)]
29. Castro, J.; Gokula Krishnan, K.; Jamaludeen, S.; Venkataragavan, P.; Gnanavel, S. Degradation and corrosion behavior of electrospun PHBV coated AZ-31 magnesium alloy for biodegradable implant applications. *J. Bio-Tribo-Corros.* **2017**, *3*, 1–7. [[CrossRef](#)]
30. Nie, K.B.; Zhu, Z.H.; Deng, K.K.; Guo, Y.C.; Han, J.G. Microstructure and tensile strength of nano-TiCp/Mg-Zn-Ca magnesium matrix nanocomposites processed by multidirectional forging. *Met. Mater. Int.* **2019**, 1–11. [[CrossRef](#)]
31. Ercetin, A. Application of the hot press method to produce new Mg alloys: Characterization, mechanical properties, and effect of Al addition. *J. Mater. Eng. Perform.* **2021**, *30*, 4254–4262. [[CrossRef](#)]
32. Ercetin, A.; Özgün, Ö.; Aslantas, K. Investigation of mechanical properties of Mg₅Sn-xZn alloys produced through new method in powder metallurgy. *J. Test. Eval.* **2021**, *49*, 3506–3518. [[CrossRef](#)]
33. Kandemir, S. Development of graphene nanoplatelet-reinforced AZ91 magnesium alloy by solidification processing. *J. Mater. Eng. Perform.* **2018**, *27*, 3014–3023. [[CrossRef](#)]
34. Kumar, J.; Singh, D.; Kalsi, N.S.; Sharma, S.; Pruncu, C.I.; Pimenov, D.Y.; Rao, K.V.; Kaplonek, W. Comparative study on the mechanical, tribological, morphological and structural properties of vortex casting processed, Al-SiC-Cr hybrid metal matrix composites for high strength wear-resistant applications: Fabrication and characterizations. *J. Mater. Res. Technol.* **2020**, *9*, 13607–13615. [[CrossRef](#)]
35. Sharma, S.; Singh, J.; Gupta, M.K.; Mia, M.; Dwivedi, S.P.; Saxena, A.; Chattopadhyaya, S.; Singh, R.; Pimenov, D.Y.; Korkmaz, M.E. Investigation on mechanical, tribological and microstructural properties of Al-Mg-Si-T6/SiC/muscovite-hybrid metal-matrix composites for high strength applications. *J. Mater. Res. Technol.* **2021**, *12*, 1564–1581. [[CrossRef](#)]
36. Donnadieu, P.; Benrhaiem, S.; Renou, G.; Zhang, C.; Tassin, C.; Blandin, J.-J. Deformation of Mg- γ Mg₁₇Al₁₂ in situ composites: Room temperature mechanical behaviour, microstructures and mechanisms. *Intermetallics* **2021**, *132*, 107127. [[CrossRef](#)]
37. Shen, M.J.; Ying, W.F.; Wang, X.J.; Zhang, M.F.; Wu, K. Development of high performance magnesium matrix nanocomposites using nano-SiC particulates as reinforcement. *J. Mater. Eng. Perform.* **2015**, *24*, 3798–3807. [[CrossRef](#)]
38. Wang, Y.; Zhang, A.; Li, G.; Liu, S.; Xiang, Y.; Cheng, H. Sintering temperature and interphase effects on mechanical properties of an oxide fiber-reinforced Al₂O₃-SiO₂ composite fabricated by Sol-Gel method. *Appl. Compos. Mater.* **2021**, *28*, 321–339. [[CrossRef](#)]
39. Dehghanian, C.; Lotfpour, M.; Emamy, M. The microstructure, and mechanical and corrosion properties of as-cast and as-extruded Mg-2%Zn-x%Cu alloys after solution and aging heat treatments. *J. Mater. Eng. Perform.* **2019**, *28*, 2305–2315. [[CrossRef](#)]
40. Lotfpour, M.; Emamy, M.; Dehghanian, C. Influence of Cu addition on the microstructure, mechanical, and corrosion properties of extruded Mg-2%Zn alloy. *J. Mater. Eng. Perform.* **2020**, *29*, 2991–3003. [[CrossRef](#)]
41. Lotfpour, M.; Emamy, M.; Dehghanian, C.; Tavighi, K. Influence of Cu addition on the structure, mechanical and corrosion properties of cast Mg-2%Zn alloy. *J. Mater. Eng. Perform.* **2017**, *26*, 2136–2150. [[CrossRef](#)]
42. Xu, H.; Zou, N.; Li, Q. Effect of ball milling time on microstructure and hardness of porous magnesium/carbon nanofiber composites. *JOM* **2017**, *69*, 1236–1243. [[CrossRef](#)]
43. Wang, T.; Huang, Y.; Yang, L.; Ma, Y.; Wu, L.; Yan, H.; Liu, Y.; Liu, W. Preparation of 2024-Al/AZ₃₁-Mg laminated composite by powder metallurgy integrated forming and sintering. *JOM* **2020**, *72*, 3547–3557. [[CrossRef](#)]
44. Erçetin, A.; Aslantaş, K.; Perçin, M. Micro milling of tungsten-copper composite materials produced through powder metallurgy method: Effect of composition and sintering temperature. *J. Fac. Eng. Archit. Gazi Univ.* **2018**, *33*, 1369–1381. [[CrossRef](#)]
45. Erçetin, A.; Aslantaş, K.; Özgün, Ö. Micro-end milling of biomedical TZ54 magnesium alloy produced through powder metallurgy. *Mach. Sci. Technol.* **2020**, *24*, 924–947. [[CrossRef](#)]
46. Nayyeri, G.; Mahmudi, R. Enhanced creep properties of a cast Mg-5Sn alloy subjected to aging-treatment. *Mater. Sci. Eng. A* **2010**, *527*, 4613–4618. [[CrossRef](#)]
47. Özgün, Ö.; Aslantaş, K.; Erçetin, A. Powder metallurgy Mg-Sn alloys: Production and characterization. *Sci. Iran.* **2020**, *27*, 1255–1265. [[CrossRef](#)]
48. Sadeghi, B.; Cavaliere, P.; Roen, G.A.; Nosko, M.; Shamanian, M.; Trembošová, V.; Nagy, Š.; Ebrahimzadeh, N. Hot rolling of MWCNTs reinforced Al matrix composites produced via spark plasma sintering. *Adv. Compos. Hybrid Mater.* **2019**, *2*, 549–570. [[CrossRef](#)]
49. Song, G.; Atrens, A. Understanding magnesium corrosion—A framework for improved alloy performance. *Adv. Eng. Mater.* **2003**, *5*, 837–858. [[CrossRef](#)]
50. Saba, F.; Sajjadi, S.A.; Heydari, S.; Haddad-Sabzevar, M.; Salehi, J.; Babayi, H. A novel approach to the uniformly distributed carbon nanotubes with intact structure in aluminum matrix composite. *Adv. Compos. Hybrid Mater.* **2019**, *2*, 540–548. [[CrossRef](#)]
51. Shouren, W.; Haoran, G.; Jingchun, Z.; Yingzi, W. Interpenetrating microstructure and properties of Si₃N₄/Al-Mg composites fabricated by pressureless infiltration. *Appl. Compos. Mater.* **2006**, *13*, 115–126. [[CrossRef](#)]
52. Ma, J.; Li, Z.J.; Xue, Y.Z.B.; Liang, X.Y.; Tan, Z.J.; Tang, B. Novel PEEK/nHA composites fabricated by hot-pressing of 3D braided PEEK matrix. *Adv. Compos. Hybrid Mater.* **2020**, *3*, 156–166. [[CrossRef](#)]
53. Suresh, S.; Gowd, G.H.; Kumar, M.L.S.D. Mechanical and wear behavior of Al 7075/Al₂O₃/SiC/mg metal matrix nanocomposite by liquid state process. *Adv. Compos. Hybrid Mater.* **2019**, *2*, 530–539. [[CrossRef](#)]

54. Shuai, C.; Zhou, Y.; Lin, X.; Yang, Y.; Gao, C.; Shuai, X.; Wu, H.; Liu, X.; Wu, P.; Feng, P. Preparation and characterization of laser-melted Mg–Sn–Zn alloys for biomedical application. *J. Mater. Sci. Mater. Med.* **2017**, *28*, 13. [[CrossRef](#)]
55. Abazari, S.; Shamsipur, A.; Bakhsheshi-Rad, H.R.; Ismail, A.F.; Sharif, S.; Razzaghi, M.; Ramakrishna, S.; Berto, F. Carbon nanotubes (CNTs)-reinforced magnesium-based matrix composites: A comprehensive review. *Materials* **2020**, *13*, 4421. [[CrossRef](#)] [[PubMed](#)]
56. Ercetin, A. A novel Mg–Sn–Zn–Al–Mn magnesium alloy with superior corrosion properties. *Metall. Res. Technol.* **2021**. [[CrossRef](#)]
57. Shahin, M.; Munir, K.; Wen, M.; Wen, C.; Li, Y. Microstructure, mechanical and corrosion properties of hot-pressed graphene nanoplatelets-reinforced Mg matrix nanocomposites for biomedical applications. *J. Alloys Compd.* **2021**, *887*, 161379. [[CrossRef](#)]
58. Munir, K.; Wen, C.; Li, Y. Graphene nanoplatelets-reinforced magnesium metal matrix nanocomposites with superior mechanical and corrosion performance for biomedical applications. *J. Magnes. Alloy.* **2020**, *8*, 269–290. [[CrossRef](#)]
59. Bakkar, A.; Neubert, V. Corrosion characterisation of alumina–magnesium metal matrix composites. *Corros. Sci.* **2007**, *49*, 1110–1130. [[CrossRef](#)]
60. Packia Antony Amalan, A.; Sivaram, N.M.; Bavatharani, C.; Ragupathy, D. A study on the effect of ageing heat treatment on hardness, tensile and corrosion behaviour of stir-cast AZ91D–5SiC–1Gr hybrid magnesium composite. *Int. J. Met.* **2021**. [[CrossRef](#)]
61. Say, Y.; Guler, O.; Dikici, B. Carbon nanotube (CNT) reinforced magnesium matrix composites: The effect of CNT ratio on their mechanical properties and corrosion resistance. *Mater. Sci. Eng. A* **2020**, *798*, 139636. [[CrossRef](#)]
62. Kumar, A.; Kumar, S.; Mukhopadhyay, N.K.; Yadav, A.; Winczek, J. Effect of SiC reinforcement and its variation on the mechanical characteristics of AZ91 composites. *Materials* **2020**, *13*, 4913. [[CrossRef](#)] [[PubMed](#)]
63. Luo, A. Processing, microstructure, and mechanical behavior of cast magnesium metal matrix composites. *Metall. Mater. Trans. A* **1995**, *26*, 2445–2455. [[CrossRef](#)]
64. Shahin, M.; Munir, K.; Wen, C.; Li, Y. Magnesium-based composites reinforced with graphene nanoplatelets as biodegradable implant materials. *J. Alloys Compd.* **2020**, *828*, 154461. [[CrossRef](#)]
65. Braszczynska-Malik, K.N.; Malik, M.A. Microstructure and mechanical properties of hypo- and hypereutectic cast Mg/Mg₂Si composites. *Materials* **2020**, *13*, 3591. [[CrossRef](#)] [[PubMed](#)]